6th International Symposium on Three-Dimensional Electromagnetics
Berkeley, California, USA, March 28-30, 2017

A vector finite element method of 3D forward modelling for CSEM with complex-shape transmitting sources

Jianhui Li[1], Colin G. Farquharson[2], Xiangyun Hu[1], and Ronghua Peng[1]
[1]China University of Geosciences, Institute of Geophysics and Geomatics, Wuhan, Hubei, China
[2]Memorial University of Newfoundland, Department of Earth Sciences, St. John's, Newfoundland, Canada

SUMMARY

A vector finite element method (VFEM), being able to make 3D forward modelling for CSEM with complex-shape sources, is presented. Any complex-shape source can be viewed as a combination of electric dipoles (EDs), each of which can be further decomposed into two horizontal EDs along the *x*- and *y*-directions, and one vertical ED along the *z*-direction. Using this method a complex-shape source can be easily handled when implementing the VFEM based on the total-field algorithm. The VFEM presented here was tested by two examples. One example was for a HED embedded in a whole-space, and the electric field was calculated using the analytic method. Then, the HED and receivers were rotated around *y*- and *z*-axes, and the electric field was calculated using the VFEM and rotated back. The results show that the analytic and numerical solutions agree well with each other. Another example was the Ovoid Zone massive sulfide ore body located at Voisey's Bay, Labrador, Canada. For this model 3D forward modelling was performed without and with the real topography. As the loop is laid on the topography surface, it means that extra VEDs are introduced compared to a horizontal loop with the same vertexes. Therefore, the model with topography presents the stronger impulse response than the one without topography.

Keywords: CSEM, 3D, vector finite element method, complex-shape source

INTRODUCTION

Electromagnetic (EM) methods are playing a more important role in mineral deposit and hydrocarbon exploration, and environmental investigations. The transmitting-source shape always presents some differences with the planned one due to a rugged topography or other natural environment influences. If these distortions are not considered in 3D forward modelling, the numerical solutions will be affected.

METHODS

The vector finite element method (VFEM), based on the total-field algorithm, is used here. The governing equation is chosen as the Helmholtz equation for the total electric field, namely

$$\nabla\times\nabla\times\mathbf{E}+i\omega\mu_0\sigma\mathbf{E}=-i\omega\mu_0\mathbf{J} \qquad (1)$$

where **E** denotes the intensity of the electric field, **J** is the electric current density of the source, σ is the conductivity, μ_0 is the permeability of free space; ω is the angular frequency. Here, the derivation process for VFEM in ommitted. The final equation based on tetrahedral grids (Li et al., 2017) is as follows

$$\sum_{e=1}^{N}\left(\sum_{j=1}^{6}E_j^e\mathbf{A}_{ij}^e+i\omega\mu_0\sigma_e\sum_{j=1}^{6}E_j^e\mathbf{B}_{ij}^e\right)=\mathbf{C} \qquad (2)$$

where E_j^e is the approximated electric field corresponding to the *j*th edge in the element *e*. $\mathbf{A}_{ij}^e=\int_{\Omega_e}\left(\nabla\times\mathbf{N}_i\right)\cdot\left(\nabla\times\mathbf{N}_j\right)d\Omega_e$, $\mathbf{B}_{ij}^e=\int_{\Omega_e}\mathbf{N}_i\cdot\mathbf{N}_j d\Omega_e$, $i=1,...,6$, N is the total number of elements, and **N** is the vector basis function. The right-hand side term **C** is $-\int_{\Omega}i\omega\mu_0\mathbf{N}_j\cdot\mathbf{J}d\Omega$, and is non-zero only for elements containing a segment of the transmitting source.

In this study a complex-shape source is viewed as a combination of electric dipoles (EDs), each of which maybe have its own direction. As shown in Figure 1, an ED can be decomposed into two horizontal EDs along *x*- and *y*-directions, and one vertical ED along *z*-direction, and the corresponding length factors are cos(β)cos(α), cos(β)sin(α) and sin(β), respectively. Given the length of the initial ED is *ds*, the electric current inside this ED can be represented as following

$$\begin{aligned}\mathbf{J}=Ids&\left(\sin\left(\beta\right)\delta\left(x-x_z\right)\delta\left(y-y_z\right)\delta\left(z-z_z\right)\mathbf{z}\right.\\&+\cos\left(\beta\right)\sin\left(\alpha\right)\delta\left(x-x_y\right)\delta\left(y-y_y\right)\delta\left(z-z_y\right)\mathbf{y}\\&\left.+\cos\left(\beta\right)\cos\left(\alpha\right)\delta\left(x-x_x\right)\delta\left(y-y_x\right)\delta\left(z-z_x\right)\mathbf{x}\right)\end{aligned} \qquad (3)$$

where (x_x, y_x, z_x), (x_y, y_y, z_y) and (x_z, y_z, z_z) are the central points for the three decomposed EDs, respectively.

To guarantee the uniqueness of the VFEM solution, the homogeneous Dirichlet boundary condition, the most practical choice for geophysical electromagnetic simulations (Um et al., 2010), was used here. A direct solver, MUMPS (Amestoy et al., 2006), was employed to solve the linear system of equations resulting from equation 2.

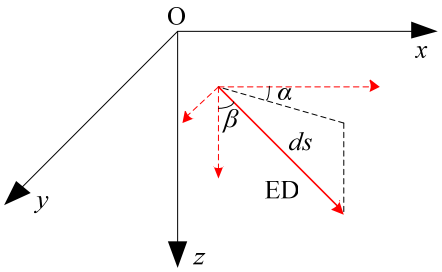

Figure 1. An ED is decomposed into two horizontal EDs along *x*- and *y*-directions, and one vertical ED along *z*-direction.

EXAMPLES

A rotated HED source

A HED source is embedded in a whole-space of conductivity 0.1 S/m or 0.001 S/m. In the Cartesian coordinate system the HED is located at the origin, and the coordinates of the two ends are (-0.5, 0.0, 0.0) m and (0.5, 0.0, 0.0) m. For the observation points, the *x*-coordinates are from -1000 to 1000 m with 100 m interval, except for 0 m, and the *y*- and *z*-coordinates are both equal to 0 m. For this scenario the analytic solutions for the EM field can be calculated using the formulas of Ward and Hohmann (1988). Then, the HED and observation points are rotated around both *y*- and *z*-axes. Based on the method of Yin and Fraser (2004), the rotated coordinates are computed by the formula

$$\mathbf{V}_a = \mathbf{D}_z \mathbf{D}_y \mathbf{V}_b \tag{4}$$

where $\mathbf{V}_b$ and $\mathbf{V}_a$ are the coordinates before and after rotating, respectively. The matrixes $\mathbf{D}_y$ and $\mathbf{D}_z$ are defined as

$$\mathbf{D}_y = \begin{pmatrix} \cos\theta & 0 & -\sin\theta \\ 0 & 1 & 0 \\ \sin\theta & 0 & \cos\theta \end{pmatrix}, \mathbf{D}_z = \begin{pmatrix} \cos\gamma & -\sin\gamma & 0 \\ \sin\gamma & \cos\gamma & 0 \\ 0 & 0 & 1 \end{pmatrix} \tag{5}$$

Here, both θ and γ are 10°. For example, the rotated coordinates of the two ends are (-0.485, 0.087, -0.086) m and (0.485, -0.087, 0.086) m. Hence, the source is no longer a HED, just an ED. When implementing the VFEM, the mesh near the ED and receivers was locally refined. In order to test the VFEM presented here, the numerical solutions should be inversely transformed into the HED scenario using the following formula

$$\mathbf{F}_a = \mathbf{D}_y^{-1} \mathbf{D}_z^{-1} \mathbf{F}_b \tag{6}$$

where $\mathbf{F}_b$ and $\mathbf{F}_a$ are the EM fields before and after inversely rotating, respectively.

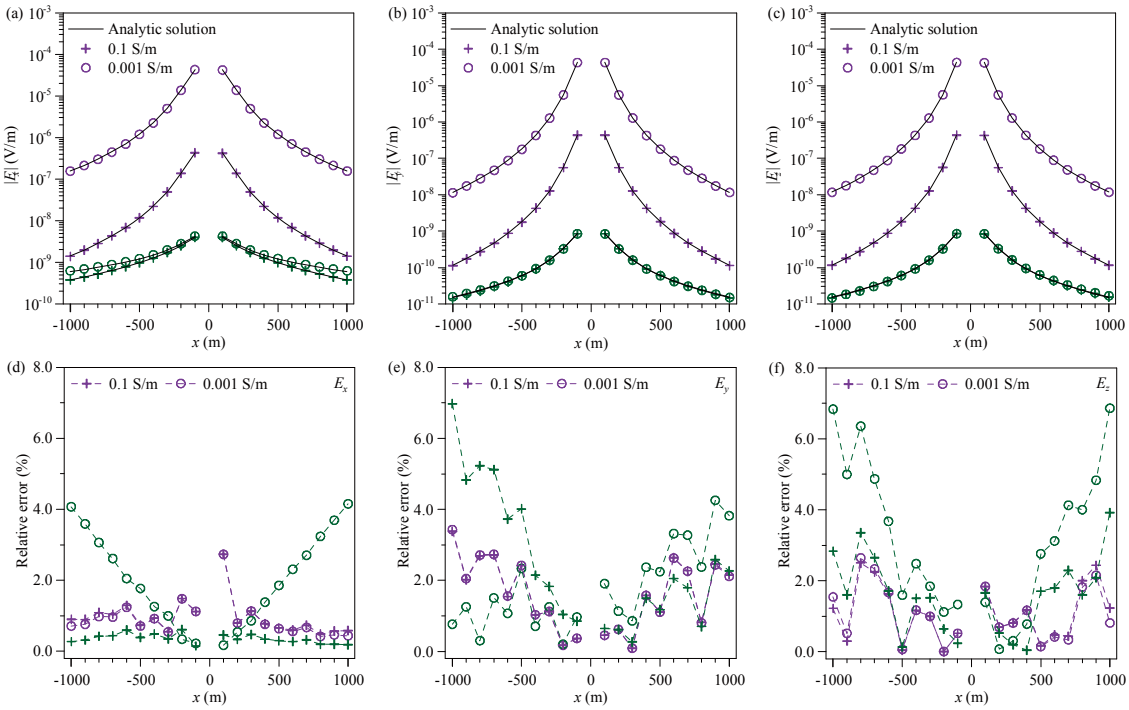

Figure 2. The VFEM solutions denoted by plus and circle for a rotated HED. Panels (a), (b) and (c) are the *x*-, *y*- and *z*-components of the electric field respectively, panels (d), (e) and (f) are the corresponding relative errors. The purple and green lines and symbols denote the real and imaginary parts of the electric field, respectively.

Figure 2 shows that the VFEM solutions for the three components of the electric field agree well with the analytic ones for both whole-spaces. Most of the relative errors are smaller than 5%, except for the imaginary parts of the *y*- and *z*-components at the larger *x*-coordinate.

A complex-shape loop source

This model is of the Ovoid Zone massive sulfide ore body located at Voisey's Bay, Labrador, Canada. According to drilling data, the Ovoid Zone is a flat-lying pod of 70% massive sulfide. It is approximately 400 m long, 300 m wide, and up to 115 m thick (Balch et al., 1998). The geometry of this ore body is shown in Figure 3(a), (b) and (c). Jahandari and Farquharson (2014) presented three-dimensional forward modelling results for this deposit model, including the real topography shown in Figure 4, for a helicopter frequency-domain EM survey. Here, we also considered this model with the topography and implemented three-dimensional forward modelling for a 500 m×500 m fixed-loop configuration and for time-domain responses. Following the experience of Jahandari and Farquharson (2014), we also set the ore body and background conductivities to 10^{2} S/m and 10^{-3} S/m, respectively. The air conductivity was set to 10^{-6} S/m.

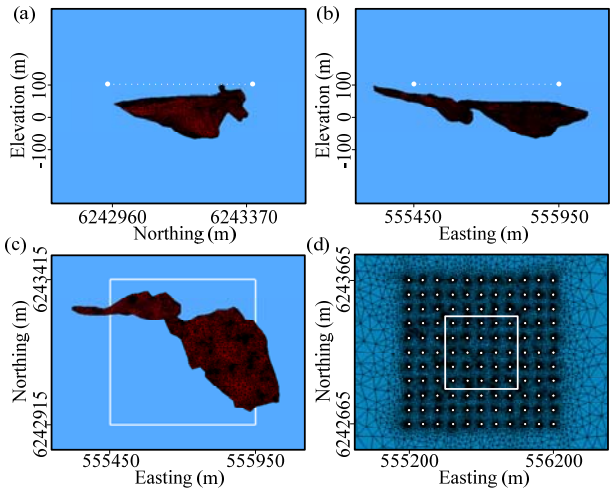

Figure 3. The tetrahedral grid of the Ovoid Zone used for the 500 m×500 m fixed-loop configuration. Panels (a) and (b) are the projection views of the ore body only onto the elevation-northing and elevation-easting planes, respectively, and panel (c) is a bird's-eye view of the ore body only. Panel (d) is the plan view for the interface between the air and the half-space (elevation=110 m) without the real topography. The white square indicates the transmitting loop, and the white points indicate the observation locations.

For both models without and with the real topography, the transmitting loop ranged from 555450 to 555950 m for the Easting coordinate, and from 6242915 to 6243415 m for the Northing coordinate. We considered a grid of 121 observation points inside and outside the transmitting loop, the positions of which are shown in Figure 3(d). The computational domain for this model was set to 50 km×50 km×50 km, and was meshed by TetGen, an open-source package of generating high-quality tetrahedral meshes (Si, 2015). The numbers of the tetrahedral edges were 1,436,554 and 1,873,344 for the models without and with the real topography, respectively. The cosine transform of Anderson (1983) with 787 coefficients were employed to calculate the time-domain responses. The range of observation times was 0.01—32.9 ms, with 35 observation times distributed evenly in terms of the logarithm of time. The frequency-domain responses were explicitly computed at 43 frequencies, distributed from 1 to 10^{7} Hz with 6 frequencies per decade.

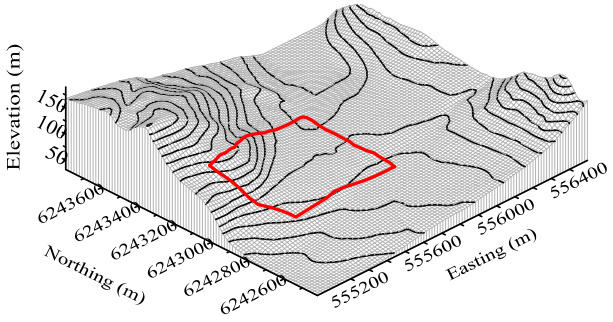

Figure 4. The real topography used for the central part of the Ovoid Zone model. The red square indicates the transmitting loop with a complex shape.

Figures 5 and 6 show the impulse response $\partial b_z/\partial t$ for the massive sulfide deposit of the Ovoid without and with the real topography. The sign-change phenomenon for the impulse response has been reported by Li et al. (2017). Here, we will mainly discuss about the effects caused by a distorted loop on the impulse responses. The most distinct characteristic is that the model with the real topography shows the stronger impulse responses for all these four times than the one without the topography. The major reason is that the observation locations are now simply closer to the ore body for the model with the real topography. In addition, the transmitting loop laid on the topography surface is viewed as a combination of EDs, each of which can be further divided into one horizontal ED and one vertical ED. The total electric moment for all the decomposed horizontal EDs is equal to the one for the loop laid on a flat surface. Therefore, the field excited by the vertical EDs is the extra part that makes the impulse responses be stronger. The second characteristic is that the shapes of the white dotted lines, indicating the boundary between the domains of positive and negative impulse responses, change also for these four times. This phenomenon is probably caused by the topography and the distorted loop together.

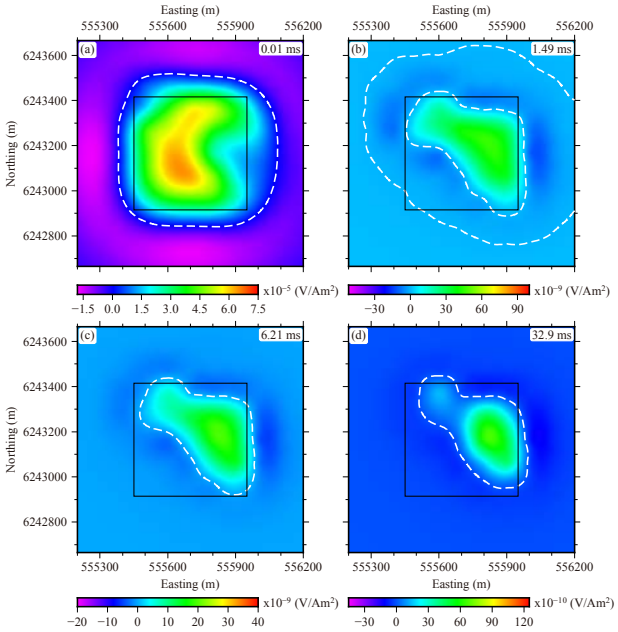

Figure 5. Contour maps of the impulse response $\partial b_z/\partial t$ for the massive sulfide Ovoid deposit without the real topography. Panels (a), (b), (c) and (d) are for the observation times 0.01, 1.49, 6.21 and 32.9 ms, respectively. The white dotted line indicates the boundary between the domains of positive and negative impulse response, and the black square indicates the transmitting loop.

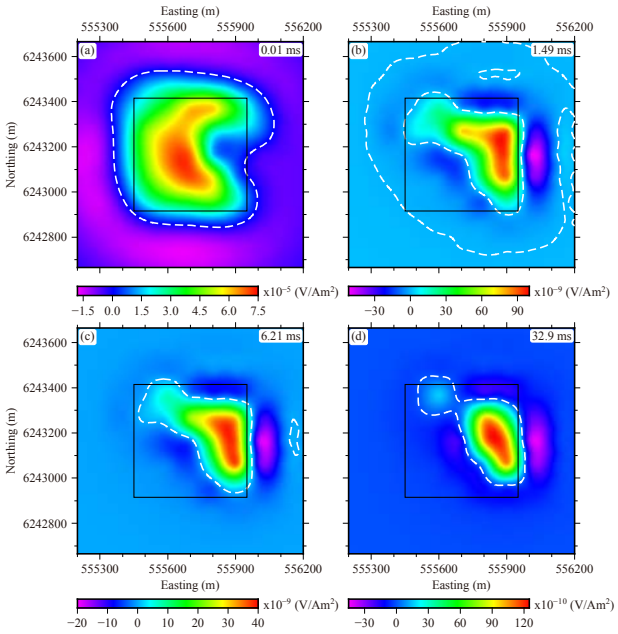

Figure 6. Same as for Figure 5, but with the real topography.

CONCLUSIONS

This paper presented an effective vector finite element method for 3D forward modelling of EM data for complex-shape transmitting sources using the total-field algorithm and unstructured tetrahedral grids. This method was illustrated using two complex-shape sources: one is a rotated HED embedded in a whole-space, for which the VFEM solutions were compared against the analytic solutions in the frequency domain, the other is a loop laid on real topography, for which the time-domain responses were considered.

ACKNOWLEDGMENTS

This work was supported by funding from the National Natural Science Foundation of China (Nos. 41504088 and 41630317).

REFERENCES

Amestoy, P. R., Guermouche, A., L'Excellent, J–Y., and Pralet, S., 2006, Hybrid scheduling for the parallel solution of linear systems, *Parallel Computing*, **32**, 136–156.

Anderson, W. L., 1983, Fourier cosine and sine transforms using lagged convolutions in double-precision (subprograms DLAGF0/DLAGF1), Technical Report 83–320, U.S. Geological Survey.

Balch, S. J., Crebs, T. J., King, A., and Verbiski, M., 1998, Geophysics of the Voisey's Bay Ni-Cu-Co deposits, SEG Technical Program Expanded Abstracts, 784–787.

Jahandari, H., and Farquharson, C. G., 2014, A finite-volume solution to the geophysical electromagnetic forward problem using unstructured grids, *Geophysics*, **79**, E287–E302.

Li, J., Farquharson, C. G., and Hu, X., 2017, 3D vector finite-element electromagnetic forward modeling for large loop sources using a total-field algorithm and unstructured tetrahedral grids, *Geophysics*, **82**, E1–E16.

Si, H., 2015, TetGen, a Delaunay-based quality tetrahedral mesh generator, *ACM Transactions on Mathematical Software*, **41**, 1–36.

Yin, C., and Fraser, D. C., 2004, Attitude corrections of helicopter EM data using a superposed dipole model, *Geophysics*, **69**, 431–439.

Um, E. S., Harris, J. M., and Alumbaugh, D. L., 2010, 3D time-domain simulation of electromagnetic diffusion phenomena: A finite-element electric-field approach, *Geophysics*, **75**, F115–F126.

Ward, S. H., and Hohmann, G. W., 1988, Electromagnetic theory for geophysical applications, *Electromagnetic methods in applied geophysics: Theory: vol. 1,* Nabighian, M. N. ed., SEG, Tulsa, 131–252.